Improvement of catalytic performance of preferential oxidation of CO in H2-rich gases on three-dimensionally ordered macro- and meso-porous Pt–Au/CeO2 catalysts

Yongxin Liu[a], Baocang Liu[a,b], Yang Liu[a], Qin Wang[a], Wenting Hu[a], Peng Jing[a], Lixia Liu[a], Shengli Yu[a], Jun Zhang[a,b,c,*]

[a] College of Chemistry and Chemical Engineering, Inner Mongolia University, Hohhot 010021, PR China
[b] College of Life Sciences, Inner Mongolia University, Hohhot 010021, PR China
[c] Inner Mongolia Key Lab of Nanoscience and Nanotechnology, Hohhot 010021, PR China

ABSTRACT

Three-dimensionally ordered macro- and meso-porous (3DOM) M/CeO2 (M = Pt, Au and Pt–Au) catalysts supported with different noble metal nanoparticles of Pt, Au and Pt–Au alloy were synthesized by thermal decomposition of cerium nitrate precursor using the close packed structures of PS colloidal crystals as templates. The obtained 3DOM M/CeO2 catalysts possess well-defined 3DOM skeletons composed of ultrafine CeO2 nanoparticles. The macroporous CeO2 skeletons contain the mesoporous walls possessing the nanopores of $\sim$3–4 nm and the noble metal nanoparticles of Pt, Au, and Pt–Au alloy with the grain sizes of $\sim$5.0 nm homogenously dispersed. The catalytic performance of CO preferential oxidation (PROX) in H2-rich gases on 3DOM Pt/CeO2, Au/CeO2, and Pt–Au/CeO2 catalysts were systematically studied. The superior catalytic performance with 90% CO conversion and 83% CO2 selectivity are realized on 3DOM 1 wt.% Pt_1Au_1/CeO2 catalyst at 80 °C under the weight hourly space velocity of 30,000 mL g^{-1} h^{-1}. Moreover, the 3DOM 1 wt.% Pt_1Au_1/CeO2 catalyst exhibits excellent catalytic stability maintaining 90% CO conversion and 56% CO2 selectivity even after the test period of 260 h under the same flow rate. The three-dimensionally ordered macro- and meso-porous skeletons, the synergistic effect due to the formation of Pt–Au alloy, and the strong interaction of Pt–Au alloy nanoparticles with CeO2 supports are identified to be beneficial to the improvement of catalytic activity and stability of CO PROX. The obtained 3DOM Pt–Au/CeO2 catalysts may be potential candidates with the improved catalytic performance of CO PROX reaction in H2-rich gases for polymer electrolyte membrane fuel cells (PEMFCs) applications.

© 2013 Elsevier B.V. All rights reserved.

1. Introduction

Polymer electrolyte membrane fuel cells (PEMFCs) have received increasing scientific interest due to their fascinating energy efficiency, superior environmental benefit and low operating temperature (80–100 °C) [1–3]. Hydrogen is the fuel of PEMFCs, and is mainly rooted in the reformate gases through coal gasification, natural gas reforming or partial oxidation [4,5]. Unfortunately, a small amount of CO in reforming streams is simultaneously formed together with H2, H2O, and CO2. Due to the presence of CO even in traces, the metal electrodes of PEMFCs, especially Pt anodes, are susceptible of poisoning and are rapidly deactivated affecting the proper operation of fuel cells. The critical requirement for PEMFCs application is to feed CO-free H2 gases to the anode. Therefore, before entering fuel cell, the CO concentration in H2 gases should be a suitable level less than 10 ppm [6,7]. In H2-rich atmosphere, the removal of CO is a great challenge. Among many strategies studied, the preferential oxidation of CO (CO PROX) that selectively oxidizes CO in excess H2 is an extremely simple and effective method to obtain clean H2 power in a wide operation temperature window (80–180 °C) for practical application of fuel cells [8–10].

The prime requirement of a good CO PROX catalyst is high activity and selectivity toward the oxidation of CO more than of H2. Numerous types of catalytic systems such as the noble metal Au [11–14], Pt [12,15], Rh [12], Ru [12,16], Pd [17] supported on different carriers, the bimetallic systems [18,19], and the mixed transition metal oxides of CuO_x-CeO2 [20–23], have been widely studied for CO PROX reaction in the presence of H2. The highly dispersed Au-based catalysts show extremely high catalytic performance at low temperature, when the size of Au particles is smaller

* Corresponding author at: Inner Mongolia University College of Chemistry and Chemical Engineering, No. 235, West University Road, Hohhot 010021, China. Tel.: +86 471 4992175; fax: +86 471 4992278.
E-mail address: cejzhang@imu.edu.cn (J. Zhang).

than 5 nm [24,25]. Hutchings et al. reported the excellent CO PROX reaction catalytic performance of Au/α-Fe_2O_3 catalysts with 99.8% CO conversion and 51% CO_2 selectivity at ~80 °C under fuel cell conditions, which succeeded in meeting the demanding performance targets (>99.5% CO conversion and >50% selectivity) for practical fuel cell application [26,11]. However, the supported Au catalysts inevitably suffer from rapid deactivation in high temperature environments. Some researchers have illustrated the crucial reasons of catalyst deactivation during CO PROX reaction under H_2-rich gases in detail [27,28], and the change of chemical states and the blockage of active sites by the formation of carbonates and H_2O are believed to be the key factors for inhibiting the CO PROX reaction. Compared to the Au-based catalysts, the supported Pt catalysts are commonly used in CO PROX reaction and often display noticeable activity at wider operating temperatures. Previous studies demonstrated that the supported Pt catalysts on different carriers showed the complete removal of CO during CO PROX reaction at temperatures above 423 K [29,30]. However, the improvement of catalytic performance that can selectively oxidize CO at low temperature is still a challenge.

The supported bimetallic catalysts reported so far, particularly the bimetallic Pt–Au nanoparticles, were of very importance for catalysis of CO PROX reaction due to their synergistic effect arisen from the formation of a new phase or alloy to suppress the adsorbed CO and change the electronic band structure to modify the strength of the surface adsorption [31], thus exhibiting superior catalytic performance at low-temperatures. Luengnaruemitchai et al. demonstrated that the Pt–Au/CeO_2 catalyst prepared by single-step sol–gel method showed superior catalytic activity than their corresponding monometallic catalysts and possessed good stability at 90 °C [32].

To date, various types of supports including activated carbon [33], zeolite [34], Al_2O_3 [35], Fe_2O_3 [36], CeO_2 [37], CeO_2-ZrO_2 [5], and CeO_2-Co_3O_4 [38] have been widely studied. Among them, CeO_2 can promote oxidation under low oxygen atmosphere, which is attributed to high oxygen storage capacity and unique redox property between Ce^{3+} and Ce^{4+} [13]. Kugai and co-workers demonstrated that CeO_2-supported catalysts possessed higher CO conversion and selectivity than Fe_2O_3-supported catalysts, due to their high capacity for oxygen transport between small CeO_2 crystallites [39].

Recently, three-dimensionally ordered macroporous (3DOM) materials have stimulated great research interest for using as catalyst supports in a variety of catalytic reactions due to their unique natures of relatively high specific surface area, large pore volume, periodical pore structure, tunable pore size, well-controlled surface characteristic, ordered channel network, and good penetrability [40]. In our previous works [41–43], 3DOM Au/CeO_2 and Au/CeO_2-Co_3O_4 catalysts were synthesized by thermal decomposition of cerium and cobalt precursors using the close packed structures of PS colloidal crystals as templates, and these catalysts showed enhanced catalytic performance in HCHO catalytic oxidation and CO PROX reaction in H_2-rich gases. However, in comparison with Au supported CeO_2 catalysts, the Pt or Pt–Au alloy supported CeO_2 catalysts are believed to be more effective for CO PROX reaction in H_2-rich gases.

In this work, we developed a series of three-dimensionally ordered macro- and meso-porous (3DOM) M/CeO_2 (M = Pt, Au, and Pt–Au) catalysts supported with different noble metal nanoparticles of Pt, Au, and Pt–Au alloy synthesized by thermal decomposition of cerium nitrate precursors using the close packed structures of PS colloidal crystals as templates. In comparison with the 3DOM Au/CeO_2 and Pt/CeO_2 catalysts, the 3DOM Pt–Au/CeO_2 catalysts show superior catalytic activity with 90% CO conversion and 83% CO_2 selectivity for CO PROX reaction in H_2-rich gases, which is much higher than our previously reported 3DOM

Au/CeO_2-Co_3O_4 catalysts [38]. The improvement of catalytic activity and stability of 3DOM Pt–Au/CeO_2 catalysts may be ascribed to the three-dimensionally ordered macro- and meso-porous skeletons, the synergistic effects derived from the formation of Pt–Au alloy, and the strong interaction of Pt–Au alloy nanoparticles with CeO_2 supports. The 3DOM M/CeO_2 catalysts possess well-defined macro- and meso-porous skeletons, which may be potential candidates for improving catalytic performance of CO PROX reaction in H_2-rich gases for polymer electrolyte membrane fuel cells (PEMFCs) applications.

2. Experimental

2.1. Catalyst preparation

2.1.1. Synthesis of 3DOM CeO_2 supports

Before the synthesis of 3DOM CeO_2 supports, mono-dispersed polystyrene (PS) spheres with average diameters of ~200 nm were synthesized by a soap-free-emulsion polymerization method and were packed into close packed structures by centrifugation, which were used as templates for the materials prepared by a sol–gel method according to our previous report [42]. Then, the 3DOM CeO_2 supports were synthesized following the procedures described below: Appropriate amounts of $Ce(NO_3)_3 \cdot 6H_2O$ precursors were dissolved in the solvent of EtOH (20 mL) to achieve the precursor solution. PS colloidal crystal templates (4 g) were carefully introduced into a Buchner funnel, to which a vacuum was applied. Then, the precursor solution was added dropwise into the funnel until the PS colloidal crystal templates were completely impregnated. The PS colloidal crystal templates impregnated with $Ce(NO_3)_3$ precursor solution were then dried at 40 °C for 40 min. The dried composites were soaked in 30 mL of oxalic acid solution (6 g oxalic acid in 30 mL of ethanol) for 5 min, and then underwent an additional vacuum filtration and drying step. The above procedures were repeated four times to ensure the complete impregnation of $Ce(NO_3)_3$ precursor solution into the interstices of PS colloidal crystal templates. Finally, the PS colloidal crystal templates were removed by the calcination at 450 °C for 5 h with the heating rate controlled at 2 °C min^{-1} to obtain 3DOM CeO_2 supports.

2.1.2. Synthesis of 3DOM Pt–Au/CeO_2 catalysts

3DOM Pt–Au/CeO_2 catalysts were prepared by a gas bubbled-assisted sol impregnation method using both $H_2PtCl_6 \cdot 6H_2O$ and $HAuCl_4 \cdot 4H_2O$ as precursors. The typical procedures for the preparation were as follows. The mixed solutions composed of a certain amount of H_2PtCl_6 precursor (1 g/L) and $HAuCl_4$ solutions (1 g/L) were diluted with 200 mL distilled water and polyvinyl alcohol (PVA, mass concentration 1 wt.%) was added as protecting agent (mass ratio of metal and PVA at 1:1), which can prevent metal nanoparticles from aggregating in the solution. After strong magnetic stirring for 10 min at ambient environment, 3DOM CeO_2 supports (0.2 g) were introduced into the mixtures. Then, 0.1 M $NaBH_4$ solution (molar ratio of metal and $NaBH_4$ at 1:5) was added rapidly and the reaction system was further vigorously bubbled with N_2 streams for 2 h following the aging for 24 h. When the solutions became clear, it was filtered and washed with abundant hot water until the Cl^- was completely removed according to a test with $AgNO_3$. For comparison, the 3DOM Pt/CeO_2 and Au/CeO_2 catalysts were prepared following the similar procedures. Finally, the obtained samples were dried at 110 °C for 12 h and then were calcined at 400 °C in air for 2 h following the reduction in 14% H_2-86% N_2 at 400 °C for 2 h before the catalytic tests. For the synthesis of bimetallic supported catalysts of Pt–Au/CeO_2, the molar ratios of Pt to Au were varied at 3:1, 2:1, 1:1, 1:2, and 1:3.

The obtained 3DOM Pt–Au/CeO$_2$ catalysts were correspondingly denoted as Pt$_3$Au$_1$/CeO$_2$, Pt$_2$Au$_1$/CeO$_2$, Pt$_1$Au$_1$/CeO$_2$, Pt$_1$Au$_2$/CeO$_2$, and Pt$_1$Au$_3$/CeO$_2$ for the purpose of discussion in the following section, respectively.

2.1.3. Synthesis of Pt–Au/CeO$_2$ powder catalysts

To compare the catalytic performance of the macro- and mesoporous catalysts with powder catalysts using traditional carriers as supports, the powder catalysts of 1 wt.% Pt/CeO$_2$, 1 wt.% Au/CeO$_2$, and 1 wt.% Pt$_1$Au$_1$/CeO$_2$ without porous structures were prepared according to the previous report [44]. The CeO$_2$ powder supports were prepared by a precipitation method. Typically, a certain amount of Na$_2$CO$_3$ solution (0.5 M) were added into to a 250 mL baker containing 200 mL of Ce(NO$_3$)$_3$ (0.05 M) solution to adjust the pH value of the solution to 9 under vigorously magnetic stirring. Then, with the adjusting of the pH value, some precipitates were gradually formed. Then, the formed precipitates were separated by centrifugation and were washed with deionized water for three times. The precipitates were finally dried in air at 80 °C for 24 h following the calcination at 500 °C for 5 h to achieve CeO$_2$ powder supports.

1 wt.% Pt$_1$Au$_1$/CeO$_2$ powder catalyst was prepared by an impregnation method. A certain amount of H$_2$PtCl$_6$ (1 g/L) and HAuCl$_4$ precursor solutions (1 g/L) was diluted with 200 mL distilled water. Then, 0.2 g CeO$_2$ powder support was introduced into the solution under magnetic stirring for 2 h and aged for 24 h. When the solution became clear, it was filtered and washed with abundant hot water until the Cl$^-$ was completely removed according to a test with AgNO$_3$. Finally, the product was dried at 110 °C for 12 h and calcined at 400 °C in air for 2 h to obtain 1 wt.% Pt$_1$Au$_1$/CeO$_2$ powder catalyst. Before the catalytic tests, the 1 wt.% Pt$_1$Au$_1$/CeO$_2$ catalyst was reduced in 14% H$_2$-86% N$_2$ at 400 °C for 2 h. For comparison, the 1 wt.% Pt/CeO$_2$ and 1 wt.% Au/CeO$_2$ powder catalysts were prepared following the similar procedures.

2.2. Characterization

Powder X-ray diffraction (XRD) was used to characterize the phase structures of 3DOM Pt/CeO$_2$, Au/CeO$_2$, and Pt–Au/CeO$_2$ catalysts. Measurements were performed using a PuXi DX3 diffractometer (China) operated at 36 kV and 20 mA with a slit of 1/2 at a scanning rate of 2° min^{-1} in a scanning range of 2θ = 10–80°, using Cu Ka radiation (λ = 0.15406 nm). Samples for XRD measurements were prepared by gently crushing the obtained products with a mortar and pestle and were placed in a quartz glass holder for characterization. Transmission electron microscopy (TEM) characterization was performed on FEI Tecnai F20 system operated at an acceleration voltage of 200 kV to evaluate the structure, geometry, pore size, and noble metal nanoparticle distribution of 3DOM CeO$_2$ catalysts. Samples for TEM analysis were prepared by drying a drop of catalyst dispersion on an amorphous carbon coated copper grid for observation. Scanning electron micrographs were recorded with a Hitachi S-4800 N scanning electron microscope (SEM) to determine the catalyst morphologies and pore sizes. Samples for SEM measurements were deposited on silicon substrates and coated with a 5 nm Pt for characterization. Surface area measurements were performed on an ASAP 2010 Brunauer–Emmett–Teller (BET) analyzer. X-ray photoelectron spectroscopy (XPS) measurements were carried out on a XSAM800 X-ray photoelectron spectrometer with an Al Ka (1486.67 eV) excitation source to determine the existence and valence states of Pt, Au, and Pt–Au in 3DOM CeO$_2$ catalysts. Actual Pt and Au contents in the catalysts were estimated with a VARIAN VISTA-MPX ICP-Mass spectrometer (MS, USA). The composition of the catalysts was measured by inductively coupled plasma-atomic emission spectrometry (ICP-AES). H$_2$-TPR was performed in a quartz microreactor. Before the analysis, all catalysts

were calcined at 400 °C in air for 2 h and then reduced in 14% H$_2$-86% N$_2$ at 400 °C for 2 h. About 100 mg catalysts were used in each measurement and pretreated with N$_2$ at 80 °C for 30 min to remove the adsorbed carbonates and hydrates. After cooling down to room temperature and introducing the reduction agent of 5% H$_2$/N$_2$ with a flow rate of 50 mL min^{-1}, the sample was heated up to 900 °C from room temperature at a rate of 10 °C min^{-1}. The H$_2$ consumption uptake during the reduction was measured using a thermal conductivity detector (TCD). The TCD was calibrated by the quantitative reduction of CuO to the metallic copper before the measurement.

2.3. Catalytic tests

The catalytic test for CO PROX reaction in H$_2$-rich streams was carried out in a continuous flow fixed-bed reactor consisting of a U-shape quartz tube (i.d. 0.6 cm) equipped on a PX 200 catalyst evaluation system (Tianjin Pengxiang Co. Ltd.) at atmospheric pressure. Then, 100 mg of the catalyst was loaded into the reactor. The gas, which had been pre-cleaned to remove H$_2$O and CO$_2$, was continuously flowed through each catalyst in the reactor. The reactor was heated to 80 °C to remove the substances adsorbed on the surface of the catalysts and subsequently cooled to room temperature. The feed stream contained 1.0 vol.% CO, 1.0 vol.% O$_2$, 50 vol.% H$_2$ (He balanced) at a total flow rate of 50 mL min^{-1} (SV = 30,000 ml g^{-1} h^{-1}). The reaction temperature was monitored using a Q-type thermocouple U-shape quartz tube containing the catalysts and controlled with a temperature controller in the same quartz tube at a heating rate of 1 °C min^{-1}. The effluent gas consisting of CO, CO$_2$ and O$_2$ was periodically analyzed online using a gas chromatograph (GC-2014C, Shimadzu) equipped with a 3 mm × 2 m stainless-steel column packed with carbon molecular sieve and a flame ionization detector (FID) with a post-column methanator, which converts CO and CO$_2$ into CH$_4$. The consumption of O$_2$ was also periodically determined online using a gas chromatograph (GC-2014C, Shimadzu) equipped with a 3 mm × 2 m stainless-steel column packed with 13× molecule sieve and a thermal conductivity detector (TCD). The activities of the catalysts were then evaluated on the basis of CO conversion, which can be calculated with the CO concentrations in the reactant gas and in the effluent gas. The selectivity of CO PROX reaction was defined as the fraction of O$_2$ consumption used for the CO oxidation to CO$_2$ over the total O$_2$ consumption. The CO conversion and CO$_2$ selectivity are calculated using the following equations:

$$\text{CO conversion} \quad (\%) = \left\{ \frac{[\text{CO}]_{in} - [\text{CO}]_{out}}{[\text{CO}]_{in}} \right\} \times 100 \qquad (1)$$

$$\text{CO}_2 \quad \text{selectivity} \quad (\%) = \left\{ 0.5 \times \frac{[\text{CO}]_{in} - [\text{CO}]_{out}}{[\text{O}_2]_{in} - [\text{O}_2]_{out}} \right\} \times 100 \qquad (2)$$

where CO$_{in}$ and O$_{2in}$ are the concentration of CO and O$_2$ in the feed stream, respectively, CO$_{out}$ and O$_{2out}$ are the concentration of CO and O$_2$ in the effluent gases, respectively.

3. Results and discussion

3.1. Catalyst characterization

3.1.1. Structure of 3 DOM M/CeO$_2$ catalysts

The XRD characterization was performed to identify the phase structures of 3DOM CeO$_2$ support and 1 wt.% M/CeO$_2$ (M = Pt, Au, and Pt–Au) catalysts synthesized using 3DOM CeO$_2$ calcined at 450 °C as support (date not shown). The characteristic diffraction peaks centered at 28.5, 33.1, 47.5, 56.3, 59.1, 69.4, 76.7 and 79.1° can be well indexed to the lattice planes of (1 1 1), (2 0 0), (2 2 0), (3 1 1), (2 2 2), (4 0 0), (3 3 1) and (4 2 0) of fluorite phase CeO$_2$ (JCPDS No:

Table 1
The BET property of 3DOM CeO_2 support and 3DOM M/CeO_2 catalysts (M = Pt, Au and Pt–Au) synthesized using 3DOM CeO_2 calcined at 450 °C as supports.

Support or catalyst	S_{BET} (m^3/g)	V_p (cm^3/g)[a]	D_p (nm)[a]
3DOM CeO_2	72	0.12	3.7
3DOM 1 wt.% Pt/CeO_2	74	0.11	3.6
3DOM 1 wt.% Au/CeO_2	77	0.12	3.7
3DOM 1 wt.% Pt_1Au_1/CeO_2	78	0.11	3.7
3DOM 1 wt.% Pt_3Au_1/CeO_2	75	0.11	3.7
3DOM 1 wt.% Pt_1Au_3/CeO_2	72	0.10	3.6

[a] Calculated from the desorption branch of the isotherm using BJH model.

Table 2
The nominal and actual Pt or Au contents in 3DOM M/CeO_2 (M = Pt, Au and Pt–Au) catalysts estimated by ICP-MS results.

Catalyst	Nominal content (wt.%)		Actual content (wt.%)	
	Pt	Au	Pt	Au
3DOM 1 wt.% Pt/CeO_2	1.0	–	0.57	–
3DOM 1 wt.% Au/CeO_2	–	1.0	–	0.47
3DOM 1 wt.% Pt_1Au_1/CeO_2	0.5	0.5	0.30	0.28

34-0394) for all catalysts. The mean particle size of CeO_2 nanoparticles deduced from the (1 1 1) lattice plane of fluorite phase CeO_2 is estimated to be ~9.3 nm. No distinct evidence of diffraction peaks of Pt, Au, Pt–Au alloy is observed in the XRD patterns of 3 DOM Pt/CeO_2, Au/CeO_2, and Pt–Au/CeO_2, implying that the Pt, Au, and Pt–Au alloy nanoparticles are less than 5 nm in size and highly dispersed on the 3DOM CeO_2 supports [45]. The XRD patterns of 1 wt.% Pt_1Au_1/CeO_2 catalyst synthesized using 3DOM CeO_2 calcined at 450, 550 and 650 °C indicate that with the increase of calcination temperature, the mean particle sizes of 3DOM CeO_2 support increase from 9.3 nm, 11.0 nm to 15.2 nm, which eventually affect the catalytic performance of the catalysts.

3.1.2. Surface area and porous structure of 3 DOM M/CeO_2 catalysts

The N_2 adsorption–desorption isotherms and Barrett–Joyner–Halenda (BJH) measurement of 3DOM CeO_2 support, 1 wt.% Pt/CeO_2, 1 wt.% Au/CeO_2, and 1 wt.% Pt_1Au_1/CeO_2 catalysts were conducted. The BET specific surface area (S_{BET}), pore sizes (D_p) and pore volumes (V_p) of the catalysts are listed in Table 1, which show almost no variation after the loading of noble metal nanoparticles. The N_2 adsorption–desorption isotherms can be classified as type IV with a H3-hysteresis loop in the relative pressure (p/p_0) range of 0.4–1.0 for all catalysts. The nearly linear middle section of the isotherms in low pressure portion is observed, which is ascribed to unrestricted monolayer or multilayer adsorption, implying that the catalysts possess a macroporous structure. When increasing the relative pressure, the large rise in adsorption may be attributed to interparticle condensation, suggesting that a large number of mesopores exist within macropore walls [46]. The corresponding pore size distribution proves that all catalysts exhibit only one narrow peak centered at ~3–4 nm (Fig. 1). No obvious difference or trend in BET properties is observed for the CeO_2 supports after deposited with various metal species. This can contribute to the ideal embedment of noble metal nanoparticles in pore channels
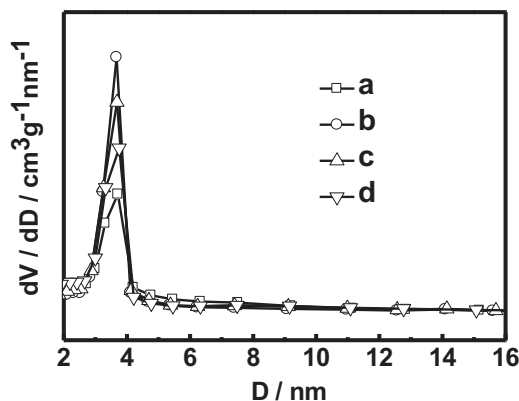
or high dispersion in supports, which are in good agreement with XRD.

3.1.3. Architecture and morphology of 3 DOM M/CeO_2 catalysts

Fig. 2 shows the TEM images of 3DOM CeO_2 support, 1 wt.% Pt/CeO_2, 1 wt.% Au/CeO_2, and 1 wt.% Pt_1Au_1/CeO_2 catalysts. The TEM images reveal that 3DOM CeO_2 support possesses a well-defined interconnected macroporous structure with pore size of ~200 nm (Fig. 2a), which is also proven by SEM characterization (Fig. S1). The magnified TEM image implies that the mesoporous structure might be existed in the macroporous skeleton of CeO_2 support due to the aggregation of ultrafine CeO_2 nanoparticles (Fig. 2b), which is further proven by Barrett–Joyner–Halenda (BJH) pore size and pore volume analysis. After loading the Pt, Au and Pt–Au alloy nanoparticles on 3DOM CeO_2 supports, the resulting 3DOM 1 wt.% Pt/CeO_2, 1 wt.% Au/CeO_2, and 1 wt.% Pt_1Au_1/CeO_2 catalysts maintain the similar morphological and structural features as 3DOM CeO_2 support (Fig. 2c–h). The existence of macro- and mesoporous structure in 3DOM Pt/CeO_2, Au/CeO_2, and Pt_1Au_1/CeO_2 catalysts is also greatly beneficial to transfer the reactants and products, which favors the improvement of catalytic performance. Moreover, the Pt, Au and Pt–Au alloy nanoparticles with the mean sizes less than 5.0 nm can be clearly observed from the HRTEM images (Fig. 2d, f and h). The HRTEM image shown in Fig. 2h further indicates that the lattice spacings of Pt–Au nanoparticles on 3DOM 1 wt.% Pt_1Au_1/CeO_2 catalyst were found to be 0.230 or 0.233 nm, which is larger than that of Pt (0.226 nm) but smaller than that of Au (0.235 nm), suggesting that the Pt–Au nanoparticles are composed of random alloy of Pt and Au, similar to that for silica supported Au–Cu alloy catalyst [47] Due to the relatively low loading contents of Pt, Au and Pt–Au alloy according to the ICP measurements (Table 2), the Pt, Au and Pt–Au alloy nanoparticles are very small and well dispersed on 3DOM CeO_2 supports. The small and well-dispersed noble metal nanoparticles may interact more strongly with CO and show higher CO oxidation activities than their corresponding larger nanoparticles and bulk entities [7].

3.1.4. Surface property of 3 DOM M/CeO_2 catalysts

XPS measurements were carried out to analyze the binding energy of Pt 4f, Au 4f and Ce 3d on the surface of 3DOM Pt/CeO_2, Au/CeO_2, and Pt–Au/CeO_2, catalysts. The XPS spectra of 3DOM 1 wt.% Pt/CeO_2, 1 wt.% Au/CeO_2, and 1 wt.% Pt_1Au_1/CeO_2 catalysts are shown in Fig. 3. For 3DOM 1 wt.% Pt/CeO_2 catalyst, the XPS profile of Pt 4f region exhibits a doublet peak at 71.25 and 74.72 eV corresponding to the characteristic of metallic Pt^0 (Fig. 3A) [45]. For 3DOM 1 wt.% Au/CeO_2 catalyst, the Au 4f signals with peaks at 83.95 and 87.59 eV are well fitted to metallic Au^0, which is slight lower than that of bulk metallic Au^0 (84.0 eV) [48] due to the formation of small Au nanoparticles and the metal-support interaction (Fig. 3B) [49]. For 3DOM 1 wt.% Pt_1Au_1/CeO_2 catalyst, the XPS spectra indicate the co-existence of Pt and Au. The spectrum of Pt 4f consists of a doublet peak at 71.58 and 74.91 eV corresponding to Pt $4f_{7/2}$ and Pt $4f_{5/2}$ of metallic Pt^0. The binding energy of Pt 4f in 3DOM 1 wt.% Pt_1Au_1/CeO_2 is higher than that in 3DOM 1 wt.% Pt/CeO_2 catalyst. Meanwhile, the doublet peaks of Au $4f_{7/2}$ and Au $4f_{5/2}$

Fig. 1. BJH measurement for the porous structures of 3DOM (a) CeO_2 support, (b) 1 wt.% Pt/CeO_2, (c) 1 wt.% Au/CeO_2 and (d) 1 wt.%Pt_1Au_1/CeO_2 catalysts.
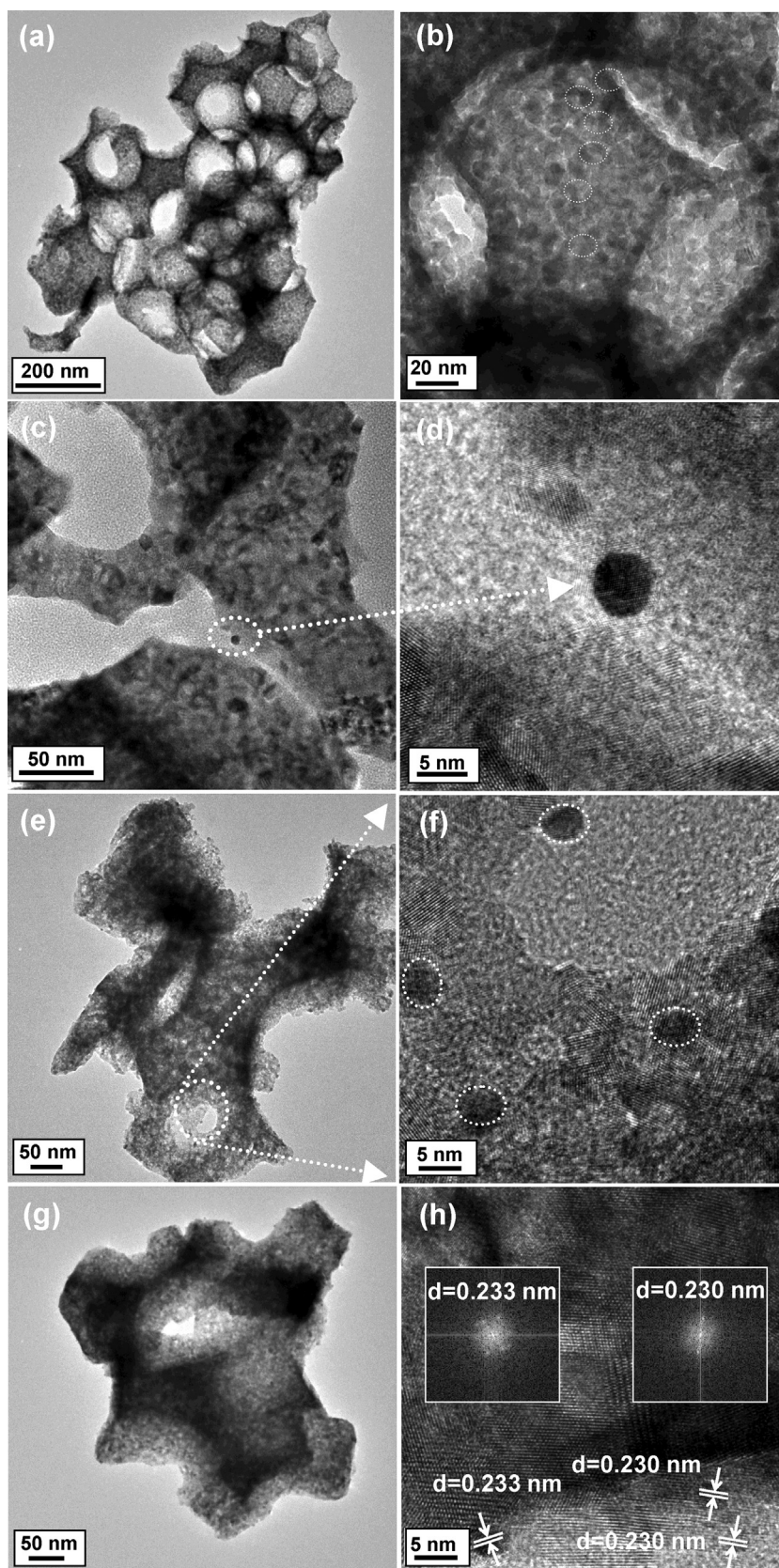
Fig. 2. TEM images of 3DOM (a and b) CeO_2 support, (c and d) 1 wt.% Pt/CeO_2, (e and f) 1 wt.% Au/CeO_2, and (g and h) 1 wt.% Pt_1Au_1/CeO_2 catalysts.
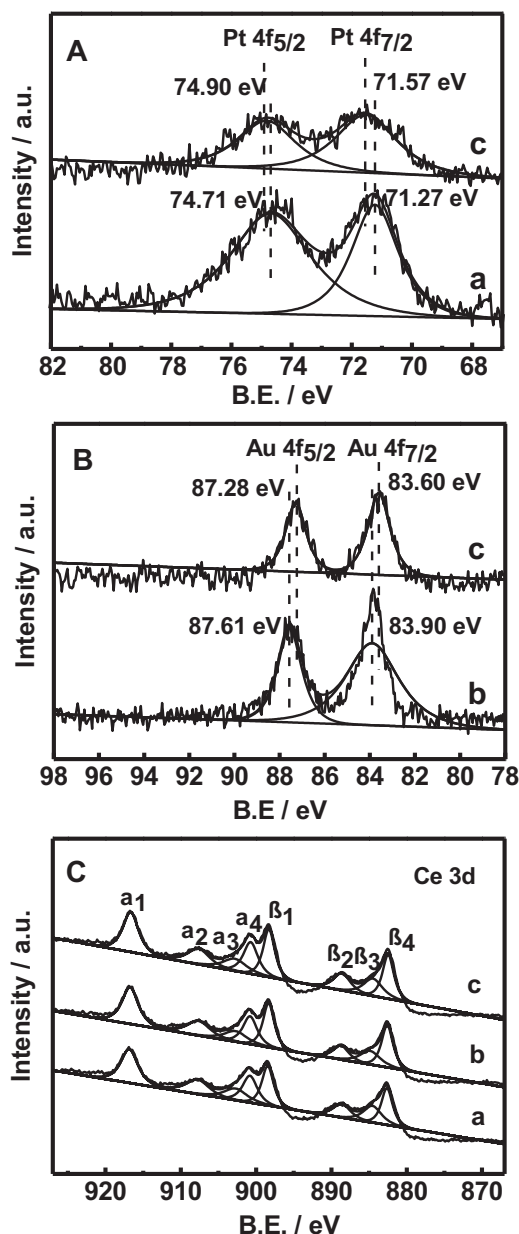
Fig. 3. Experimental and fitted XPS spectra of (A) Pt 4f, (B) Au 4f, and (C) Ce 3d of 3DOM (a) 1 wt.% Pt/CeO$_2$, (b) 1 wt.% Au/CeO$_2$ and (c) 1 wt.% Pt$_1$Au$_1$/CeO$_2$ catalysts.

Fig. 4. H$_2$-TPR profiles of 3DOM (a) CeO$_2$, (b) 1 wt.% Pt/CeO$_2$, (c) 1 wt.% Au/CeO$_2$ and (d) 1 wt.% Pt$_1$Au$_1$/CeO$_2$ catalysts.

for the Ce 3d3/2 and Ce 3d5/2 of Ce^{3+} [54]. The presence of Ce^{3+} implies the defect structure of CeO$_{2-x}$ due to oxygen vacancies. The bimetallic Pt–Au alloy nanoparticles well dispersed on the surface of the catalysts may improve the reduction capability of Ce^{4+} to Ce^{3+}. The transformation of Ce^{4+} to Ce^{3+} driven by oxygen vacancies may be the key factor that affects the catalytic properties of CeO$_2$ [55].

3.1.5. Reducibility of 3 DOM M/CeO$_2$ catalysts

H$_2$-TPR profiles of 3DOM CeO$_2$, 1 wt.% Pt/CeO$_2$, 1 wt.% Au/CeO$_2$, and 1 wt.% Pt$_1$Au$_1$/CeO$_2$ for studying their reducibility are shown in Fig. 4. The H$_2$-TPR profile of 3 DOM CeO$_2$ support shows two main reduction peaks in the range of 300–900 °C, which are assigned to the reduction of surface oxygen (436–430 °C) and the removal of bulk oxygen (708–683 °C) of CeO$_2$, respectively. In comparison, the reduction peaks of 3DOM 1 wt.% Pt/CeO$_2$, 1 wt.% Au/CeO$_2$, and 1 wt.% Pt$_1$Au$_1$/CeO$_2$ are shifted to a lower temperature than those of pure CeO$_2$ [56]. This is ascribed to the improvement of the surface reduction of Ce^{4+} to Ce^{3+} in the presence of noble metal. The 3DOM 1 wt.% Pt/CeO$_2$ catalyst exhibits a wide reduction temperature in the range of 150–300 °C. With regard to 3 DOM 1 wt.% Au/CeO$_2$ catalyst, a broadened peak occurs at 190.3 °C, which can be related to the reduction of surface oxygen of CeO$_2$ support activated by Au nanoparticles [57]. The H$_2$-TPR profile of 3DOM 1 wt.% Pt$_1$Au$_1$/CeO$_2$ catalyst is a little different from those of either 3DOM 1 wt.% Pt/CeO$_2$ or 1 wt.% Au/CeO$_2$, indicating the lower reduction temperature at 153.2 °C. This phenomenon may be an indication of a strong interaction between the Pt and Au and the bimetallic Pt–Au favors the weakening of the surface oxygen on CeO$_2$, thereby improving the reducibility of the catalyst. The interaction between the Pt and Au may form a Pt–Au alloy, resulting in a lower reduction temperature. To further confirm the existence of the interaction of Au, Pd, or Pd-Au nanoparticles with CeO$_2$ support, the H$_2$ consumption of the reduction peaks on 3DOM 1 wt.% Pt/CeO$_2$, 1 wt.% Au/CeO$_2$ and 1 wt.% Pt$_1$Au$_1$/CeO$_2$ catalysts at low temperature are measured (Table S1). It can been seen that the actual H$_2$ consumption is higher than theoretical H$_2$ consumption calculated by assuming all present as Au^{3+} and Pt^{4+} in the catalyst, implying a co-reduction of CeO$_2$ due to a typical H$_2$ spillover effect [41]. The H$_2$ consumption demonstrates that the superficial reducibility of 3DOM 1 wt.% Pt/CeO$_2$, 1 wt.% Au/CeO$_2$ and 1 wt.% Pt$_1$Au$_1$/CeO$_2$ catalysts is greater than that of CeO$_2$ support. The improvement of the superficial reducibility is beneficial for improving the catalytic activity. The results are in good agreement with the results previously reported [32,58], which explain that the excellent performance of the bimetallic catalyst is due to the formation of a Pt–Au alloy.

at 83.60 eV and 87.24 eV in 3DOM 1 wt.% Pt$_1$Au$_1$/CeO$_2$ are smaller than those in 3DOM 1 wt.% Au/CeO$_2$ catalyst. These results suggest the formation of metallic bonds between Pt and Au to form Pt–Au alloy. It is well-known that the presence of Pt–Au alloy affects the charge transfer from Pt to Au due to the higher electronegativity of Au (2.54) in relation to Pt (2.2), resulting in the increase of d-orbital vacancies in Pt [50,51]. Moreover, the reduction in intensity of XPS spectrum in bimetallic 3DOM 1 wt.% Pt$_1$Au$_1$/CeO$_2$ catalyst further explains the formation of Pt–Au alloy [52]. These properties greatly affect the catalytic activity and selectivity of the catalyst for CO PROX reaction in H$_2$-rich streams. The XPS spectra in the Ce 3d region features eight peaks dividing into two groups as α1, α2, α3, α4 and β1, β2, β3, β4 [53]. The XPS binding energies at 916.7, 907.6, and 900.7 eV corresponding to α1, α2, and α4, and the XPS binding energies at 898.3, 888.6, and 882.5 eV indexed to β1, β2, β4 refer to the Ce 3d3/2 and Ce 3d5/2 of Ce^{4+}. While the binding energies at 903.2 and 884.7 eV assigned to α3 and β3 stand
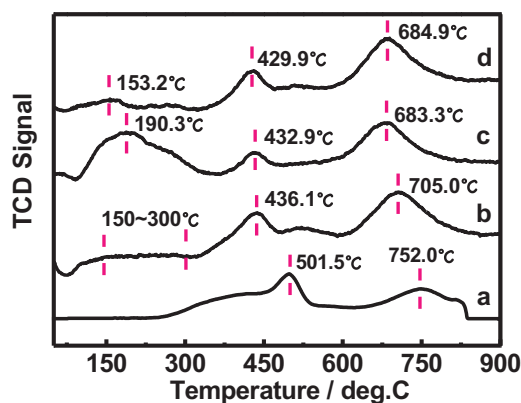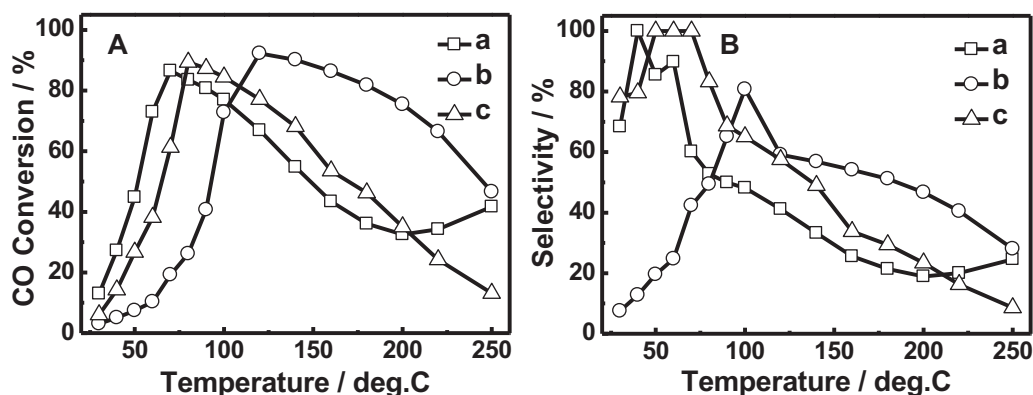
Fig. 5. (A) CO conversion and (B) CO_2 selectivity of CO PROX reaction in H_2-rich gases on 3DOM (a) 1 wt.% Pt/CeO_2, (b) 1 wt.% Au/CeO_2, (c) 1 wt.% Pt_1Au_1/CeO_2 catalysts.

3.2. Catalytic performance

3.2.1. Catalytic activity test of 3 DOM M/CeO₂ catalysts

The catalytic activity of 3DOM 1 wt.% Pt/CeO_2, 1 wt.% Au/CeO_2, and 1 wt.% Pt_1Au_1/CeO_2 catalysts for CO PROX reaction in H_2-rich gases is tested. The 1 wt.% Pt/CeO_2, 1 wt.% Au/CeO_2, and 1 wt.% Pt_1Au_1/CeO_2 catalysts show superior catalytic activity for CO PROX reaction in H_2-rich gases in the low temperature range of 30–250 °C. The evolution of CO conversion and CO_2 selectivity of CO PROX reaction in H_2-rich gases on different catalysts is shown in Fig. 5. The maximum of 87% CO conversion is achieved for 1 wt.% Pt/CeO_2 catalyst at 70 °C, and the maximum of 92% CO conversion is obtained for 1 wt.% Au/CeO_2 catalyst at 120 °C, indicating that Pt and Au supported catalysts show the difference in reaction temperature for CO PROX reaction in H_2-rich gases. In comparison, the 1 wt.% Pt_1Au_1/CeO_2 catalyst shows the excellent catalytic performance on CO PROX reaction in H_2-rich gases with 90% of CO conversion at 80 °C (Fig. 5A), which is greatly improved in comparison with the CO conversion at 80 °C for 1 wt.% Pt/CeO_2 and 1 wt.% Au/CeO_2 catalyst. The improvement of catalytic performance of CO PROX reaction in H_2-rich gases on 1 wt.% Pt_1Au_1/CeO_2 catalysts at 80 °C may be attributed to the formation of ultrafine Pt–Au alloy and the strong interaction of Pt–Au nanoparticles with CeO_2 supports. When the Pt and Au are co-existed, the Pt sites are active centers to remove CO impurities and the Au sites most likely activate O_2 to promote CO oxidation [59,60]. The maximum of 100% CO_2 selectivity is achieved for 1 wt.% Pt/CO_2 catalyst at 50 °C, and the maximum of 81% CO_2 selectivity is obtained for 1 wt.% Au/CO_2 catalyst at 100 °C (Fig. 5B). In comparison, the maximum of 100% CO_2 selectivity is attained for 1 wt.% Pt_1Au_1/CeO_2 catalyst at 70 °C. With the increasing of the reaction temperatures, the CO_2

selectivity decreases sharply (Fig. 5B). The CO_2 selectivity on 3DOM 1 wt.% Pt_1Au_1/CeO_2 catalyst decreases from 83% to 34% in the low temperature range of 80–160 °C.

Our results show that 3DOM 1 wt.% Pt_1Au_1/CeO_2 catalyst possesses the higher catalytic performance for CO PROX reaction in H_2-rich gases with 90% CO conversion and 83% CO_2 selectivity than the 3DOM 1 wt.% Pt/CeO_2 and 1 wt.% Au/CeO_2 catalysts in low operating temperature of 80 °C for practical application of fuel cells. The CO_2 selectivity of different catalysts follows in the order: 3DOM 1 wt.% Pt_1Au_1/CeO_2 > 3DOM 1 wt.% Pt/CeO_2 > 3DOM 1 wt.% Au/CeO_2 with the CO_2 selectivity of 83%, 53% and 49% at 80 °C, respectively. The highest CO_2 selectivity at 80 °C for 3DOM 1 wt.% Pt_1Au_1/CeO_2 may be due to the formation of metallic bonds between Pt and Au to form Pt–Au alloy. The presence of Pt–Au alloy affects the charge transfer from Pt to Au due to the higher electronegativity of Au (2.54) in relation to Pt (2.2), resulting in the increase of d-orbital vacancies in Pt. This may enhance the capability of Pt–Au alloy absorbing the CO and improve their CO_2 selectivity.

To compare the differences on the catalytic activity and selectivity of the macro- and meso-porous and powder catalysts, the powder catalysts of 1 wt.% Pt/CeO_2, 1 wt.% Au/CeO_2, and 1 wt.% $Pt_1–Au_1/CeO_2$ without porous structures are prepared and their catalytic performance is tested. Fig. 6 shows the catalytic activity and selectivity of 1 wt.% Pt/CeO_2, 1 wt.% Au/CeO_2, and 1 wt.% Pt_1Au_1/CeO_2 powder catalysts, which Exhibit 80%, 78% and 87% of the maximum CO conversion and 55%, 47%, and 59% of the maximum CO_2 selectivity at 70, 120, and 90 °C, respectively, which are relatively lower than that of 3DOM 1 wt.% Pt/CeO_2, 1 wt.% Au/CeO_2, and 1 wt.% Pt_1Au_1/CeO_2 catalysts. The results suggest that 3DOM M/CeO₂ (M = Au, Pd, and Pd-Au) show relatively high catalytic
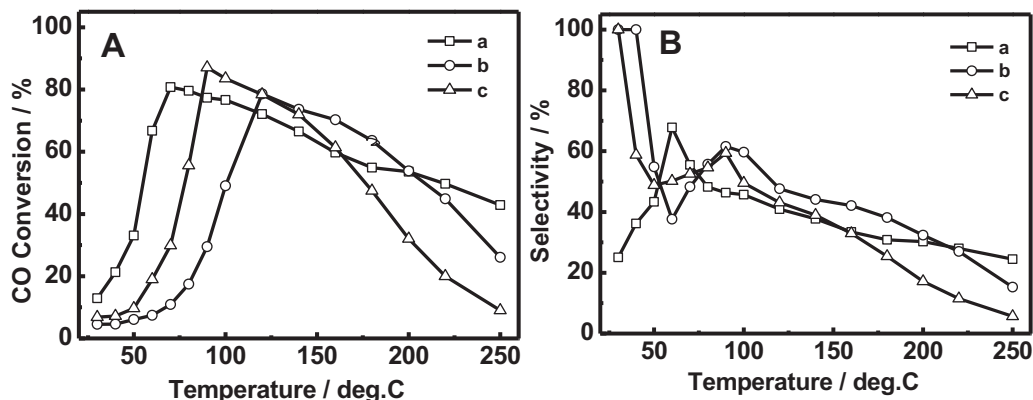

Fig. 6. (A) CO conversion and (B) CO_2 selectivity of CO PROX reaction in H_2-rich gases on powder catalysts of (a) 1 wt.% Pt/CeO_2, (b) 1 wt.% Au/CeO_2 and (c) 1 wt.% Pt_1Au_1/CeO_2.
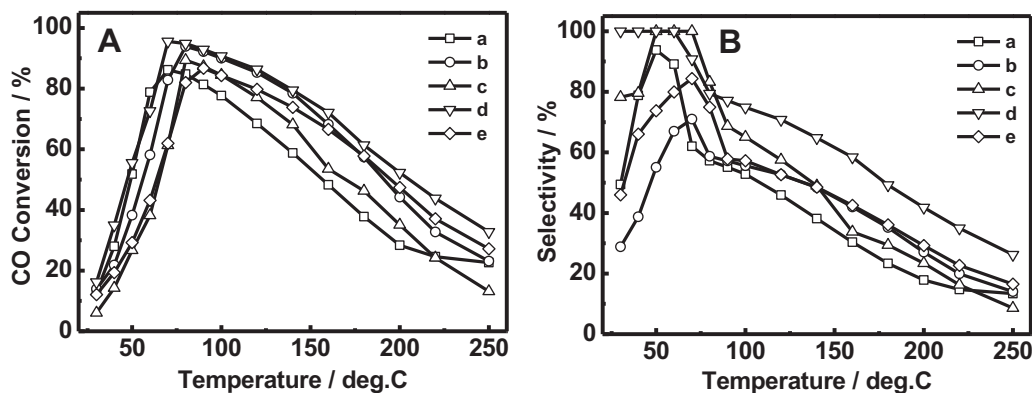
Fig. 7. (A) CO conversion and (B) CO_2 selectivity of CO PROX reaction in H_2-rich gases on 3DOM (a) 1 wt.% Pt_3Au_1/CeO_2, (b) 1 wt.% Pt_2Au_1/CeO_2, (c) 1 wt.% Pt_1Au_1/CeO_2, (d) 1 wt.% Pt_1Au_2/CeO_2 and (e) 1 wt.% Pt_1Au_3/CeO_2 catalysts.

activity and selectivity than M/CeO_2 (M = Au, Pd, and Pd–Au) powder catalysts due to their macro- and meso-porous structures.

To compare the effects of loading contents of noble metals on CO PROX, the catalytic performance of CO PROX reaction in H_2-rich gases on a series of 3 DOM Pt/CeO_2, Au/CeO_2 and Pt_1Au_1/CeO_2 catalysts with different noble metal loading contents at 1, 2, 3, and 4 wt.% are tested (Figs. S2, 3 and 4). With the increase of noble metal loading content, the maximum CO conversion is reduced slightly. Interestingly, the initial temperatures of transformation of CO to CO_2 are quite different for 3DOM Pt/CeO_2, Au/CeO_2 and Pt_1Au_1/CeO_2 catalysts. It occurs below 100 °C for 3DOM Pt/CeO_2 and Pt_1Au_1/CeO_2 catalysts, but above 100 °C for Au/CeO_2 catalyst, indicating the effective catalytic performance for Pt and Pt–Au supported catalysts than Au supported catalysts.

Fig. 7 represents the catalytic performance of 3DOM 1 wt.% Pt–Au/CeO_2 catalysts with various molar ratios of Pt and Au at 3:1, 2:1, 1:1, 1:2, and 1:3, respectively. Among the five Pt–Au bimetallic catalysts, 3DOM 1 wt.% Pt_1Au_2/CeO_2 catalyst exhibits the best catalytic performance with 96% CO conversion and 91% CO_2 selectivity at 70 °C. It can be found that the reaction temperatures of the best catalytic performance over each catalyst occur at 60–90 °C range. Comparing the catalytic activities of these catalysts at 80 °C, the CO conversion follows the order of 3DOM 1 wt.% Pt_1Au_2/CeO_2 > 1 wt.% Pt_2Au_1/CeO_2 > 1 wt.% Pt_1Au_1/CeO_2 > 1 wt.% Pt_1Au_3/CeO_2 > 1 wt.% Pt_3Au_1/CeO_2, corresponding to 95%, 94%, 90%, 85% and 82%, respectively. Moreover, the CO_2 selectivity over these catalysts is 80%, 59%, 83%, 58% and 62%, respectively. The highest CO_2 selectivity of 83% is achieved for 1 wt.% Pt_1Au_1/CeO_2 catalyst. This can be explained that the strong

synergistic effect of Pt–Au alloy due to replace partial Pt atoms with Au atoms can enhance catalytic activity.

The effects of weight hourly space velocities (WHSV) on the catalytic activity of 3DOM Pt_1Au_1/CeO_2 catalyst are studied. Fig. 8 gives the profile of CO conversion and CO_2 selectivity on 3DOM 1 wt.% Pt_1Au_1/CeO_2 catalyst at different WHSV of 18,000, 30,000, 60,000, and 90,000 $cm^3 g_{cat}^{-1} h^{-1}$. The results display clearly that the CO conversion and CO_2 selectivity drop significantly with the increase of WHSV below 120 °C. However, the CO conversion and CO_2 selectivity show a similar trend at different WHSV above 120 °C. This indicates that the reaction is not diffusion-limited under our experiment conditions. The high WHSV leads to the short contact time between the reactants and the catalysts and causes the incomplete reaction of the reactants on catalyst surfaces. Under the WHSV of 18,000 $cm^3 g_{cat}^{-1} h^{-1}$, 95% CO conversion can be obtained at 80 °C. When increasing the WHSV to 30,000 $cm^3 g_{cat}^{-1} h^{-1}$, only 90% CO conversion can be obtained at 80 °C. As the WHSV is doubled to 60,000 $cm^3 g_{cat}^{-1} h^{-1}$, the temperature of maximum CO conversion shifts slight toward high reaction temperature (90 °C). However, when the WHSV is tripled to 90,000 $cm^3 g_{cat}^{-1} h^{-1}$, it only presents a CO conversion of 70% at 120 °C. The CO_2 selectivity falls from 83% to 43% with the increase of WHSV under 120 °C.

The effects of particle sizes of CeO_2 supports on the catalytic activity of the catalysts are also investigated. Fig. 9 shows the CO conversion and CO_2 selectivity of CO PROX reaction on 3DOM 1 wt.% Pt_1Au_1/CeO_2 synthesized using 3DOM CeO_2 calcined at different temperatures of 450, 550, and 650 °C as supports The dramatic loss of catalytic activity for 3DOM Pt_1Au_1/CeO_2 catalyst synthesized using 3DOM CeO_2 calcined at 550 and 650 °C temperatures
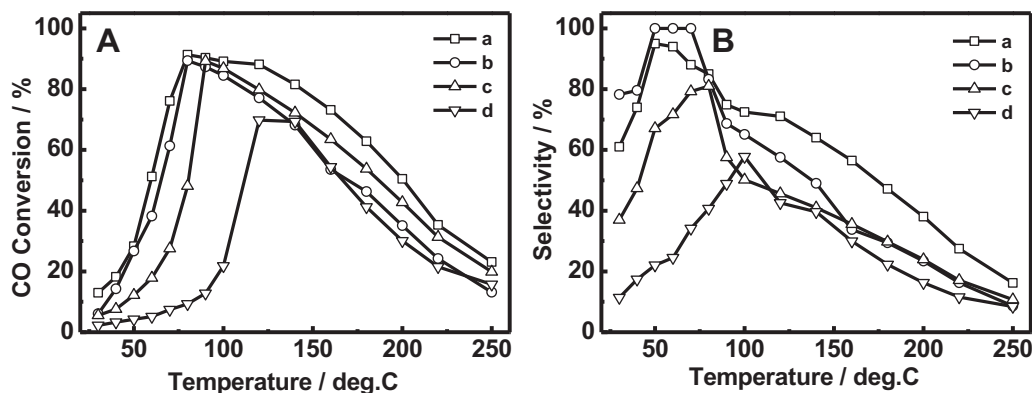

Fig. 8. (A) CO conversion and (B) CO_2 selectivity of CO PROX reaction in H_2-rich gases on 3DOM 1% Pt_1Au_1/CeO_2 performed under different space velocities of (a) 18,000, (b) 30,000, (c) 60,000 and (d) 90,000 mL g^{-1} h^{-1}.
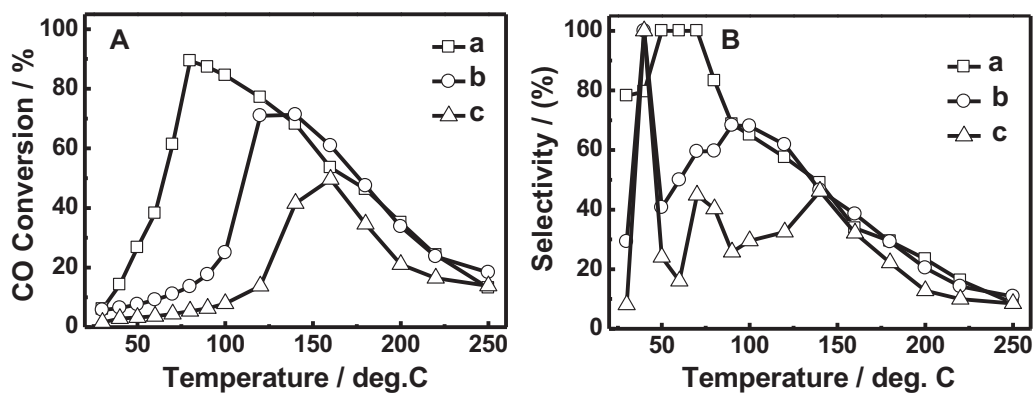
Fig. 9. (A) CO conversion and (B) CO_2 selectivity of CO PROX reaction in H_2-rich gases on 3DOM 1 wt.% Pt_1Au_1/CeO_2 synthesized using 3DOM CeO_2 calcined at different temperatures of (a) 450, (b) 550 and (c) 650 °C as supports.

as supports is observed, which can be interpreted as the gradual enlargement of particle sizes of CeO_2 supports with the increase of calcination temperature. Therefore, the increment of particle sizes of CeO_2 supports may result in the reduction of the amounts of reactants interacting with the active centers. Consequently, the decrease of catalytic activity is unavoidable.

3.2.2. Catalytic stability test of 3 DOM M/CeO₂ catalysts

To further evaluate the catalytic stability, the catalytic performance of CO-PROX in H_2-rich gases on 3DOM 1 wt.% Pt_1Au_1/CeO_2 catalyst is tested for 260 h at a low temperature of 80 °C, at which the practical PEFMCs are operated. The evolution of CO conversion and CO_2 selectivity with time on stream (TOS) are depicted in Fig. 10. It is indicated that the long-term stability of 3DOM 1 wt.% Pt_1Au_1/CeO_2 catalyst with 90% CO conversion rate is attained even after 260 h running period, and no obvious decline in CO conversion is observed. However, the CO_2 selectivity drops drastically from 100% to 62% during the first 24 h, and then has the partial loss in the next 72 h, ultimately maintaining steady at 56% in the following hours. This result prevails over the previous report [32], in which the long-term stability lifetime over Pt_1Au_1/CeO_2 catalyst is obtained for 13 h at 90 °C with removal CO of 90% and CO_2 selectivity of approximately 47%. The possible reason for the remarkable lifetime improvement may be attributed to the well-defined interconnected macro- and meso-porous structures of 3DOM 1 wt.% Pt_1Au_1/CeO_2 catalyst. This is quite different from the previously reported Pt_1Au_1/CeO_2 catalyst without porous structures [32], since the 3DOM Pt_1Au_1/CeO_2 catalyst with

mesoporous walls can transfer the reactant species and waste produced rapidly during the reaction.

3.2.3. Deactivation of 3 DOM M/CeO₂ catalysts

To investigate the deactivation of 3DOM 1 wt.% Pt_1Au_1/CeO_2 catalyst, the FT-IR of the fresh and used 3DOM 1 wt.% Pt_1Au_1/CeO_2 catalyst are performed. Fig. 11 presents the FT-IR spectra of the fresh and used 3DOM 1 wt.% Pt_1Au_1/CeO_2 catalysts. It is worth noted that two peaks in the used catalyst appear at 1049 and 1114 cm^{-1}, which correspond to the C—O stretching vibration (νCO_3^{2-}) of carbonate and hydrocarbonate absorbed on surface of CeO_2. The formation of carbonate and hydrocarbonate on catalyst surface would largely affect the catalytic performance. As a consequence, they may cause the deactivation of the catalyst.

Furthermore, to confirm the change of Pt–Au alloy on the surface of 3DOM 1 wt.% Pt_1Au_1/CeO_2 catalysts that accounts for deactivation of the catalysts after longtime stability test, XPS characterization was performed. Fig. 12 shows the XPS spectra of Pt 4f and Au 4f of the fresh and used 3DOM 1 wt.% Pt_1Au_1/CeO_2 catalysts. It can be deduced for the XPS data that the Pt and Au contents on the surface of the fresh 3DOM 1 wt.% Pt_1Au_1/CeO_2 catalyst is estimated to be 0.35% and 0.28%. After the longtime stability tests, the Pt and Au contents on the surface of the used 3DOM 1 wt.% Pt_1Au_1/CeO_2 catalyst is approximately 0.28% and 0.25%. The metallic Pt species decrease significantly in the used 3DOM 1 wt.% Pt_1Au_1/CeO_2 catalyst; while the metallic Au species reduce weakly. These results suggest that during the catalytic performance, the Pt–Au alloy on the surface of the catalyst is reconstructed. The Pt nanoparticles deplete fast and cause the loss of the activity sites for CO conversion, therefore, leading to the decrease of activity of the catalysts after
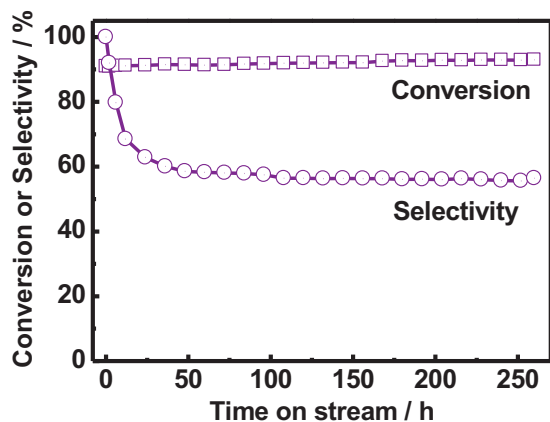

Fig. 10. The evolution of CO conversion and CO_2 selectivity with time on stream on 3DOM 1 wt.% Pt_1Au_1/CeO_2 catalyst for CO PROX reaction in H_2-rich gases. Reaction temperature: 80 °C; Reaction gas: 1.0% CO, 1.0% O_2, 50.0% H_2 and He (balance); Space velocity: 30,000 mL g^{-1} h^{-1}.
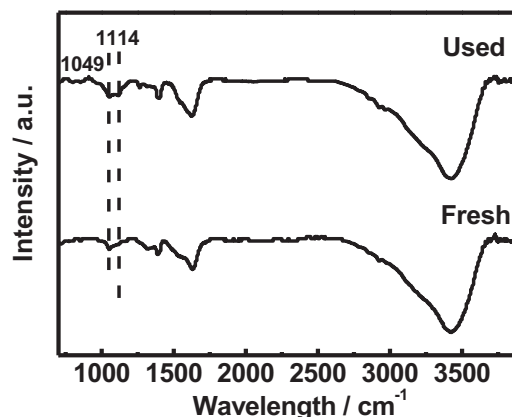

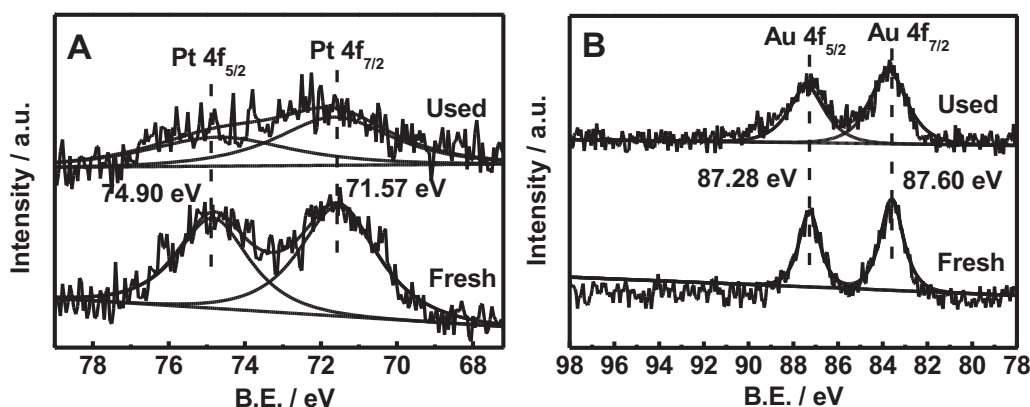**Fig. 11.** FT-IR spectra of the fresh and used 3DOM 1 wt.% Pt_1Au_1/CeO_2 catalysts.

Fig. 12. Experimental and fitted XPS spectra of Pt 4f (A) and Au 4f (B) of the fresh and used 3DOM 1 wt.% Pt_1Au_1/CeO_2 catalysts.

longtime stability test [28]. Meanwhile, with the increase of reaction temperatures, the selectivity also drops due to the competition of H_2 with CO at higher temperatures.

4. Conclusions

In summary, a series of 3DOM M/CeO_2 (M = Pt, Au and Pt–Au) catalysts were synthesized by thermal decomposition of cerium nitrate precursor using the close packed structures of PS colloidal crystals as templates, and their catalytic performance for CO PROX reaction in H_2-rich gases was systematically studied. The obtained 3DOM M/CeO_2 catalysts possess well-defined macroporous CeO_2 skeletons with mesoporous walls composed of ultrafine CeO_2 nanoparticles and well-dispersed noble metal nanoparticles. The catalytic performance shows that the 3DOM Pt–Au/CeO_2 catalysts loaded with bimetallic Pt–Au alloy nanoparticles exhibit superior catalytic performance than 3DOM Pt/CeO_2 and Au/CeO_2 catalysts supported with monometallic Pt and Au nanoparticles. The 3DOM 1 wt.% Pt_1Au_2/CeO_2 catalyst with Pt and Au loading content ratio at 1:1 shows the superior catalytic performance with 90% CO conversion and 83% CO_2 selectivity at 80 °C, and the long-term stability lifetime of 3DOM 1 wt.% Pt_1Au_1/CeO_2 catalyst can be realized with 90% CO conversion and 56% CO_2 selectivity even after the period of 260 h running time. The well-defined interconnected macro- and meso-porous structure, the enhanced synergistic effect due to the formation of ultrafine Pt–Au alloy nanoparticles, and the strong interaction between Pt–Au alloy nanoparticles and CeO_2 supports may account for the improvement of catalytic performance of CO PROX reaction in H_2-rich gases. The low temperature activity, high selectivity and durable stability of 3DOM Pt–Au/CeO_2 catalyst make them potentially applicable in CO PROX reaction in H_2-rich gases for practical PEMFCs application.

Acknowledgment

Appendix A. Supplementary data

Supplementary data associated with this article can be found, in the online version, at http://dx.doi.org/10.1016/j.apcatb.2013.06.002.

References

[1] S. Ahmed, M. Krumpelt, International Journal of Hydrogen Energy 26 (2001) 291–301.
[2] B.C.H. Steele, A. Heinzel, Nature 414 (2001) 345.
[3] J. Wu, X.Z. Yuan, J.J. Martin, H. Wang, J. Zhang, J. Shen, S.W. Wu, Merida 184 (2008) 104.
[4] J.D. Holladay, J. Hu, D.L. King, Y. Wang, Catalysis Today 139 (2009) 244.
[5] Z. Zhao, X. Lin, R. Jin, Y. Dai, G. Wang, Catalysis Communication 12 (2011) 1448.
[6] N. Perkas, J. Teo, S. Shen, Z. Wang, J. Highfield, Z. Zhong, A. Gedanken, Physical Chemistry Chemical Physics 13 (2011) 15690.
[7] I.H. Son, M. Shamsuzzoha, A.M. Lane, Journal of Catalysis 210 (2002) 460.
[8] J.W. Desmond Ng, Z. Zhong, J. Luo, A. Borgna, International Journal of Hydrogen Energy 35 (2010) 12724.
[9] F. Mariño, C. Descorme, D. Duprez, Applied Catalysis B: Environmental 54 (2004) 59.
[10] E.D. Park, D. Lee, H.C. Lee, Catalysis Today 139 (2009) 28.
[11] P. Landon, J. Ferguson, B.E. Solsona, T. Garcia, A.F. Carley, A.A. Herzing, C.J. Kiely, S.E. Golunski, G.J. Hutchings, Chemical Communications (2005) 3385.
[12] M. Kipnis, E. Volnina, Applied Catalysis B: Environmental 98 (2010) 193.
[13] O. Pozdnyakova, D. Teschner, A. Wootsch, J. Kröhnert, B. Steinhauer, H. Sauer, L. Toth, F.C. Jentoft, A. Knop-Gericke, Z. Paál, R. Schlögl, Journal of Catalysis 237 (2006) 1.
[14] M. Kipnis, E. Volnina, Applied Catalysis B: Environmental 103 (2011) 39.
[15] T. Takei, T. Akita, I. Nakamura, T. Fujitani, M. Okumura, K. Okazaki, J. Huang, T. Ishida, M. Haruta, Advances in Catalysis 55 (2012) 1.
[16] Y.H. Kim, J.E. Park, H.C. Lee, S.H. Choi, E.D. Park, Applied Catalysis B: Environmental 127 (2012) 129.
[17] I. Miguel-García, Á. Berenguer-Murcia, D. Cazorla-Amorós, Applied Catalysis B: Environmental 98 (2010) 161.
[18] B.D. Chandler, A.B. Schabel, L.H. Pignolet, Journal of Catalysis 193 (2000) 186.
[19] Y.H. Wang, J.L. Zhu, J.C. Zhang, L.F. Song, J.Y. Hu, S.L. Ong, W.J. Ng, Journal of Power Sources 155 (2006) 440.
[20] L.F. Liotta, G. Di Carlo, G. Pantaleo, A.M. Venezia, Catalyis Today 158 (2010) 56.
[21] S. Scire, P.M. Riccobene, C. Crisafulli, Applied Catalysis B: Environmental 101 (2010) 109.
[22] G. Yi, H. Yang, B. Li, H. Lin, K. Tanaka, Y. Yuan, Catalysis Today 157 (2010) 83.
[23] S.K. Mehera, M. Cargnello, H. Troiani, T. Montini, G.R. Rao, P. Fornasiero, Applied Catalysis B: Environmental 130–131 (2013) 121.
[24] V. Aguilar-Guerrero, B.C. Gates, Journal of Catalysis 260 (2008) 351.
[25] Y.-W. Chen, H.-J. Chen, D.-S. Lee, Journal of Molecular Catalysis A: Chemical 363–364 (2012) 470.
[26] P. Landon, J. Ferguson, B.E. Solsona, T. Garcia, S. Al-Sayari, A.F. Carley, A.A. Herzing, C.J. Kiely, M. Makkee, J.A. Moulijn, A. Overweg, S.E. Golunski, G.J. Hutchings, Journal of Materials Chemistry 16 (2006) 199.
[27] X. Li, S.S.S. Fang, J. Teo, Y.L. Foo, A. Borgna, M. Lin, Z. Zhong, ACS Catalysis 2 (2012) 360.
[28] H. Wang, H. Zhu, Z. Qin, F. Liang, G. Wang, J. Wang, Journal of Catalysis 264 (2009) 154.
[29] E.O. Jardim, M. Gonçalves, S. Rico-Francés, A. Sepúlveda-Escribano, J. Silvestre-Albero, Applied Catalysis B: Environmental 113–114 (2012) 72.
[30] M.M.V.M. Souza, N.F.P. Ribeiro, M. Schmal, International Journal of Hydrogen Energy 32 (2007) 425.
[31] J. Luo, P.N. Njoki, Y. Lin, D. Mott, C.-J. Wang, Zhong, Langmuir 22 (2006) 2892.
[32] S. Monyanon, S. Pongstabodee, A. Luengnaruemitchai, Journal of Power Sources 163 (2006) 547.
[33] S. Lu, Y. Liu, Applied Catalysis B: Environmental 111–112 (2012) 492.
[34] V. Sebastian, S. Irusta, R. Mallada, J. Santamaría, Applied Catalysis A: General 366 (2009) 242.
[35] Y.H. Kim, E.D. Park, Applied Catalysis B: Environmental 96 (2010) 41.
[36] M.M. Schubert, A. Venugopal, M.J. Kahlich, V. Plzak, R.J. Behm, Journal of Catalysis 222 (2004) 32.

[37] O.H. Laguna, F. Romero Sarria, M.A. Centeno, J.A. Odriozola, Journal of Catalysis 276 (2010) 360.
[38] Q. Guo, Y. Liu, Applied Catalysis B: Environmental 82 (2008) 19.
[39] J. Kugai, T. Moriya, S. Seino, T. Nakagawa, Y. Ohkubo, H. Nitani, Y. Mizukoshi, T.A. Yamamoto, Applied Catalysis B: Environmental 126 (2012) 306.
[40] Y. Zhang, H. Liang, X.Y. Gao, Y. Liu, Catalysis Communications 10 (2009) 1432.
[41] B. Liu, Y. Liu, C. Li, W. Hu, P. Jing, Q. Wang, J. Zhang, Applied Catalysis B: Environmental 127 (2012) 47.
[42] Y. Liu, B. Liu, Q. Wang, C. Li, W. Hu, Y. Liu, P. Jing, W. Zhao, J. Zhang, Journal of Catalysis 296 (2012) 65.
[43] J. Zhang, Y. Jin, C. Li, Y. Shen, L. Han, Z. Hu, X. Di, Z. Liu, Applied Catalysis B: Environmental 91 (2009) 11.
[44] Y. Shen, X. Yang, Y. Wan, Y. Zhang, H. Zhu, L. Gao, M. Jia, Applied Catalysis B: Environmental 79 (2008) 142–148.
[45] K.-J. Kim, H.-G. Ahn, Applied Catalysis B: Environmental 91 (2009) 308.
[46] G. Zhang, Z. Zhao, J. Xu, J. Zheng, J. Liu, G. Jiang, A. Duan, H. He, Applied Catalysis B: Environmental 107 (2011) 302.
[47] X. Liu, A. Wang, T. Zhang, D. Su, C. Mou, Catalysis Today 160 (2011) 103–108.
[48] Y.-C. Bai, W.-D. Zhang, C.-H. Chen, J.-Q. Zhang, Journal of Alloys and Compounds 509 (2011) 1029.
[49] R. Leppelt, B. Schumacher, V. Plzak, M. Kinne, R.J. Behm, Journal of Catalysis 244 (2006) 137.
[50] L. Zhang, A.M. Karim, M.H. Engelhard, Z. Wei, D.L. King, Y. Wang, Journal of Catalysis 287 (2012) 37.
[51] G. Selvarani, S.V. Selvaganesh, S. Krishnamurthy, G.V.M. Kiruthika, P. Sridhar, S. Pitchumani, A.K. Shukla, Journal Physical Chemistry C 113 (2009) 7461.
[52] B.N. Wanjala, J. Luo, R. Loukrakpam, B. Fang, D. Mott, P.N. Njoki, M. Engelhard, H.R. Naslund, J.K. Wu, L. Wang, O. Malis, C.-J. Zhong, Chemistry of Materials 22 (2010) 4282.
[53] S. Mandal, A.B. Mandale, M. Sastry, Journal of Materials Chemistry 14 (2004) 2868.
[54] J. Li, Y. Han, Y. Zhu, R. Zhou, Applied Catalysis B: Environmental 108–109 (2011) 72.
[55] Q. Dai, S. Bai, Z. Wang, X. Wang, G. Lu, Applied Catalysis B: Environmental 126 (2012) 64.
[56] Q. Yu, W. Chen, Y. Li, M. Jin, Z. Suo, Catalysis Today 158 (2010) 324.
[57] J.D.S.L. Fonseca, H.S. Ferreira, N. Bion, L.M. Pirault-Roy, d.C. Rangel, D. Duprez, F. Epron, Catalysis Today 180 (2012) 34.
[58] D.J. Suh, C. Kwak, J.-H. Kim, S.M. Kwon, T.-J. Park, Journal Power Sources 142 (2005) 70.
[59] F. Wang, D. Zhang, Y. Ding, Journal Physical Chemistry C 114 (2010) 14076.
[60] S. Zhou, K. McIlwrath, G. Jackson, B. Eichhorn, Journal of the American Chemical Society 128 (2006) 1780.